



Short communication

Interplay between two-phase and solid solution reactions in high voltage spinel cathode material for lithium ion batteries

Jie Xiao ^{a,*}, Xiqian Yu ^{b,1}, Jianming Zheng ^a, Yungang Zhou ^a, Fei Gao ^a, Xilin Chen ^a, Jianming Bai ^b, Xiao-Qing Yang ^b, Ji-Guang Zhang ^{a,*}^a Pacific Northwest National Laboratory, Richland, WA 99352, USA^b Brookhaven National Laboratory, Upton, NY 11973, USA

H I G H L I G H T S

- Explore the fundamental roles of element doping in high voltage spinel.
- Provide direct evidences for the interplay between two-phase and solid solution reactions.
- Correlate the structural modification with the electrochemical property in spinel.

A R T I C L E I N F O

Article history:

Received 4 February 2013

Received in revised form

21 May 2013

Accepted 28 May 2013

Available online 6 June 2013

Keywords:

Two-phase reaction

Solid solution

High voltage spinel

Lithium ion battery

Energy storage

A B S T R A C T

Lithium ion batteries (LIBs) are attracting intensive interests worldwide because of their potential applications in transportation electrification and utility grid. The intercalation compounds used in LIBs electrochemically react with Li^+ ions via single or multiple phase transitions depending on the nature of the material structure as well as the synthesis and operating conditions. For $\text{LiNi}_{0.5}\text{Mn}_{1.5}\text{O}_4$ high voltage spinel, a promising candidate positive electrode material for LIBs, there are three spinel-structured phases sequentially appeared through two successive two-phase reactions during the delithiation/lithiation processes. Here we demonstrate, experimentally and theoretically, that through elemental substitution, the solid solution ranges for both the first and second phases are significantly extended during the electrochemical charge–discharge process. This type of structural changes with more solid solution regions facilitate fast Li^+ diffusion by reducing the number of phase boundaries that Li^+ ions have to overcome and resulted in less shrinkage of the unit cells at the end of charge process. This work unravels the fundamental interactions between structural and electrochemical properties by using spinel as the platform, which may be widely adopted to explain or tailor the properties of materials for energy storage and conversion.

© 2013 Elsevier B.V. All rights reserved.

In the effort of increasing the energy density of LIBs for vehicle and electric grid applications, the lack of satisfied high energy positive electrode materials is the “bottleneck” [1,2]. The theoretical capacities of intercalation compounds usually used in LIBs are determined by the number of Li^+ ions per transition metal ion, that can reversibly deintercalate/intercalate in the crystal structure. However, it is quite challenging to design new structures that can sustainably deliver high capacity through multi-electron reactions [3]. The operating voltage, another factor in energy density, is related to the Fermi energy of each electrode material [4]. The

operating voltage as well as the voltage curve, i.e. sloped or flat plateau, depend on the chemical composition, crystal structure, and reaction mechanism of the specific electrode [5]. Interestingly, the reaction pathway for some materials can be changed through different methodologies. For example, tailoring LiFePO_4 particles to nano sizes and generating Li/Fe anti-site mixing in the lattice can narrow the miscibility gap and increase the solid solution range [6]. When heated at 450 °C, two metastable phases of $\text{Li}_{0.75}\text{FePO}_4$ and $\text{Li}_{0.5}\text{FePO}_4$ can be emerged into a single phased solid solution [7]. A recent interesting paper also mentioned that the simultaneous occurrence of solid solution and two-phase reactions in commercial LiFePO_4 under non-equilibrium conditions controlled by the electrochemical potentials [8].

In contrast to LiFePO_4 , another promising positive electrode material, $\text{LiNi}_{0.5}\text{Mn}_{1.5}\text{O}_4$, received much less attention in terms of its phase transition mechanism [9,10]. $\text{LiNi}_{0.5}\text{Mn}_{1.5}\text{O}_4$ operates at a

* Corresponding authors. Tel.: +1 509 3754598; fax: +1 509 3752186.

E-mail addresses: jie.xiao@pnnl.gov (J. Xiao), ji-guang.zhang@pnnl.gov (J.-G. Zhang).¹ These authors contributed equally to this work.

high voltage of ca. 4.7 V and therefore providing more energy density than traditional positive electrode materials such as LiCoO_2 or LiFePO_4 [11]. Several groups including ours have reported the effects of synthetic routes, [12–19] control of calcination process [20–22] or elemental doping [23–26], on improving the electrochemical performances of $\text{LiNi}_{0.5}\text{Mn}_{1.5}\text{O}_4$. However, it is still unclear how the mechanistic and dynamic processes change after lattice modulation, for example, through elemental substitution. Slight changes of the charge–discharge curves have been clearly observed for doped spinels in the literature [27,28], which suggests the alteration of the reaction mechanism of spinel during delithiation/lithiation. However, so far there is still not enough information to confirm this speculation.

In this work, we present direct evidences for the interplay between two-phase and solid solution reactions by using Cr-doped high voltage spinel as a platform. This work clarifies the fundamental roles of elemental doping/substitution in high voltage spinels and correlates the lattice changes to the electrochemical behaviors, which is then further explained through theoretical simulations.

1. Experimental

$\text{LiNi}_{0.5}\text{Mn}_{1.5}\text{O}_4$ and $\text{LiNi}_{0.45}\text{Mn}_{1.5}\text{Cr}_{0.05}\text{O}_4$ was prepared according to our earlier report [26]. After high temperature synthesis, both samples were further heated again at 700 °C for another 12 h.

In situ X-ray diffraction (XRD) patterns were collected at beam line X14A of National Synchrotron Light Source (NSLS, BNL) by a linear position sensitive silicon detector. The wavelength used was 0.77376 Å. X-ray absorption spectroscopy (XAS) experiments were performed at X-18A beamline at NSLS in transmission mode using a Si (111) double-crystal monochromator detuned to the 35–45% value of its original maximum intensity to eliminate the high order harmonics. X-ray Absorption Near Edge Structure (XANES) and Extended X-ray Absorption Fine Structure (EXAFS) data were analysed by ATHENA software package [29]. The EXAFS data analysis was carried out using standard procedures. The normalized k^3 -weighted EXAFS spectra were Fourier transformed (FT) in k space with integration limits of 3.1–11 Å^{−1} for the Mn data and Ni data. Structural parameters were obtained by nonlinear least-squares analysis of the data using phase and amplitude functions generated from FEFF6 code [30]. The least-square fits were carried out in R space between 1 Å^{−1} and 2.9 Å^{−1} using FIFFIT. The amplitude reduction factor S_0^2 was scaled to a value of 0.67 for the Mn edge and 0.8 for the Ni edge, respectively, after preliminary refinements. The structure parameter for specific absorbers, Debye–Waller factor, was extracted by curve fitting. All of the fitting R -factor values were less than 0.05, indicating reliable fitting results. Morphology of spinel electrodes with different carbon additives was observed with a FEI Helios scanning electron microscope (SEM).

The optimized cell cans, separators, carbon additives and electrolyte identified in our recent studies have been used in this work [31,32]. Positive electrodes were prepared by coating a mixture containing 80% $\text{LiNi}_{0.5}\text{Mn}_{1.5}\text{O}_4$, 10% super P (from Timcal), and 10% poly(vinylidene fluoride) (PVDF, Kynar HSV900, Arkema Inc.) binder onto Al current collector foil. After drying, the electrodes were punched into disks with $\phi = 1.27$ cm. The active material loading was 3–5 mg cm^{−2}. Coin cells were assembled in an argon-filled MBraun glove box by using lithium foil as anode and Celgard K1640 monolayer polyethylene (PE) membrane as separator. 1 M lithium hexafluorophosphate (LiPF_6) dissolved in ethyl carbonate (EC) and dimethyl carbonate (DMC) (3:7 in volume) was used as electrolyte. The button cells were galvanostatically cycled between 3.2 and 4.9 V on an Arbin BT-2000 battery tester at room temperature (22–23 °C) at 1C (1C = 140 mA g^{−1}). Cyclic voltammogram (CV) was performed between 3.2 and 5.1 V at 50 $\mu\text{V s}^{-1}$.

1.1. Modeling

Vienna ab initio simulation package (VASP) is used for Density functional theory (DFT) calculations. The $\text{Li}_x\text{Ni}_{0.5}\text{Mn}_{1.5}\text{O}_4$ system is modeled in a supercell that contains 4 Ni atoms, 12 Mn atoms, 32 O atoms and 8x Li atoms ($0 < x < 1$). The electronic wave functions were expanded using plane-wave basis set with a cutoff energy of 550 eV and the Brillouin zone integration was performed using $6 \times 6 \times 6$ k-point grid. In order to account for the electron localization around the transition metal ions, the $+U$ scheme was employed with the U values of 5.9, 3.0 and 4.5 for Ni, Cr and Mn atoms, respectively.

2. Results and discussion

$\text{LiNi}_{0.5}\text{Mn}_{1.5}\text{O}_4$ and its Cr-doped counterpart $\text{LiNi}_{0.45}\text{Cr}_{0.05}\text{Mn}_{1.5}\text{O}_4$, discussed throughout this work, are synthesized by the same approach. Post-synthesis heating were applied on both spinels to minimize the influences from oxygen deficiency [19]. The high voltage spinels are both comprised of homogeneously distributed micron sized particles (Fig. S1). The morphology similarities rule out factors other than Cr-doping, which might potentially affect the reaction pathways of spinel. *In situ* XRD analysis is performed on pure and Cr-doped spinels during charge or delithiation (Fig. 1). For undoped $\text{LiNi}_{0.5}\text{Mn}_{1.5}\text{O}_4$ (Fig. 1a), annealing process renders this

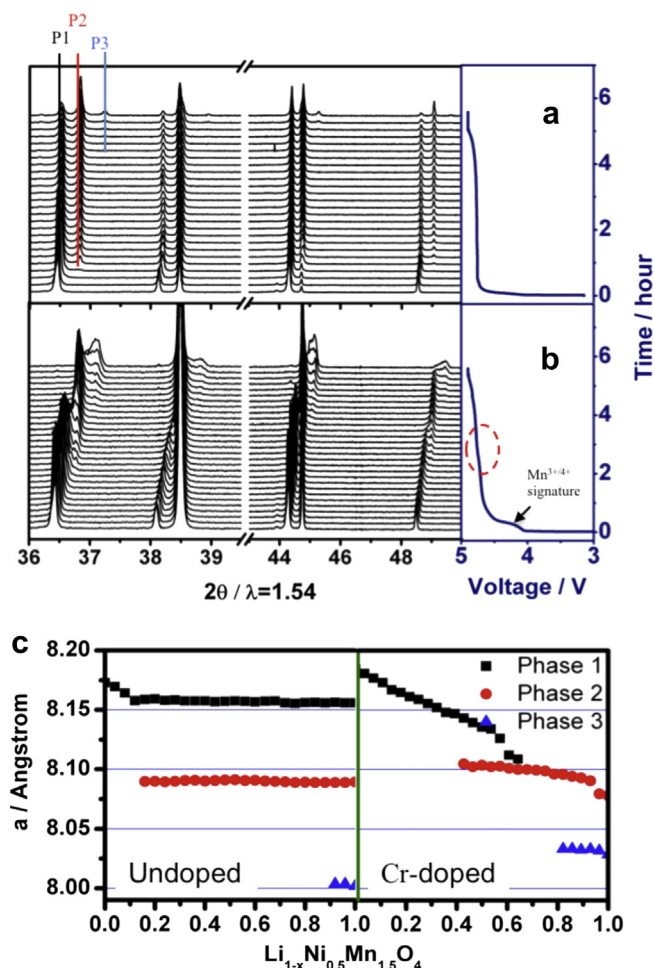


Fig. 1. *In situ* XRD patterns of a) $\text{LiNi}_{0.5}\text{Mn}_{1.5}\text{O}_4$ and b) $\text{LiNi}_{0.45}\text{Cr}_{0.05}\text{Mn}_{1.5}\text{O}_4$ during charge (electrochemical delithiation) processes. The corresponding voltage profiles at different SOC are also plotted. c) Compares the changes of lattice parameters of both spinels at different SOC.

material with a dominated $P4_332$ crystallographic structure, [18,25,33] consistent with the negligible signature plateau for Mn^{3+} at ca.4.0 V (Fig. 1a). Three different spinel phases in Fig. 1a, i.e. $LiNi_{0.5}Mn_{1.5}O_4$ (P1), $Li_{0.5}Ni_{0.5}Mn_{1.5}O_4$ (P2) and $Ni_{0.5}Mn_{1.5}O_4$ (P3), clearly appeared sequentially at different states of charge (SOC), representing the two-step 2-phase transitions (P1 to P2 and P2 to P3) between three cubic phases. Once charge process is initiated, P2 appears quickly in the first two-phase reaction region. It is interesting to note the continuous decrease of lattice parameter in the very beginning of charge (Fig. 1c: left), which may indicate a very short-range of one-phase reaction at this initial charge state of $LiNi_{0.5}Mn_{1.5}O_4$. Similar phenomenon was reported in nano-size $LiFePO_4$ [6]. The occurrence of P3 is somewhat delayed, so a constant voltage step at 4.9 V is used in Fig. 1a. This may be partially related with the incomplete conversion from P1 to P2, both of which still exist even at the end of the charge in Fig. 1a. $LiNi_{0.5}Mn_{1.5}O_4$ in Fig. 1a is mainly comprised of ordered phase [26] and has to experience two consecutive two-phase reactions during charge–discharge. In contrast to solid solution reaction, Li^+ ions have to overcome numerous phase boundaries to complete each of the two-phase transitions, slowing down the electrochemical process. The sluggish kinetic properties associated with the multi-phase transition in Fig. 1a are therefore caused by material itself and impede the Li^+ diffusion, partially responsible for the inferior electrochemical performances of $P4_332$ -type high voltage spinel reported in literature [19,22,26]. After substituting 5% Ni with Cr, however, the occurrence scenario of these three cubic phases during delithiation has been changed completely. In Fig. 1b, up to 40% of SOC, a solid solution reaction dominates. P2 occurs and coexists with P1 from 40% to 60% of SOC in Fig. 1b, followed by another solid solution reaction associated with P2 covered from 60% to 80% of SOC, while P1 completely disappears at this stage. P3 only appears after 80% of SOC, indicating that the second two-phase transition range is also largely pushed back to SOC close to the end of the charge (Fig. 1b). In addition, the corresponding charge curve in Fig. 1b witnesses a more sloped plateau, a signature of solid solution reaction, compared to the much flatter one in Fig. 1a. The step between the two plateaus on the charging curve corresponding P1/P2 and P2/P3 transitions in doped spinel (circled in Fig. 1b) is also much more observable than in the undoped one (Fig. 1a). After discharge, both spinels completely convert back into the individual original phases (Fig. S2), suggesting that Li^+ intercalation/deintercalation process is quite reversible in the spinel crystalline at moderate current density (C/5 rate for *in situ* XRD experiment).

The corresponding lattice constant changes of $LiNi_{0.5}Mn_{1.5}O_4$ and $LiNi_{0.45}Cr_{0.05}Mn_{1.5}O_4$ at different SOC were further compared in

Fig. 1c. Lattice parameter “*a*” stays almost constant for each cubic phase during charge for the undoped $LiNi_{0.5}Mn_{1.5}O_4$. However, for Cr-doped spinel, P1 demonstrates a continuous decrease of “*a*” before the sample is delithiated to a composition of $Li_{0.4}Ni_{0.45}Cr_{0.05}Mn_{1.5}O_4$. Although P2 also appears after extracting 0.4 mol of Li^+ , the solid solution range of P1 coexists with the P2 (two-phase reaction) from $0.6 \geq Li \geq 0.4$ region, suggesting a concurrent occurrence of both reaction pathways within this range. After 60% of SOC, the continuous decrease of *a* for P2 (Fig. 2c) is consistent with the earlier discussion in Fig. 1, where the second solid solution reaction takes over, followed by another P2/P3 two-phase region between $0.2 \geq Li \geq 0$. Of note, at the end of the charge, the change of lattice constant from P1 to P3 in Cr-doped spinel is much less than that of the undoped parent, probably related with the reduced shrinkage of the unit cell in Cr-doped spinel, which is further supported by the extended EXAFS results below.

The Fourier transformed *ex situ* EXAFS spectra for $LiNi_{0.5}Mn_{1.5}O_4$ and $LiNi_{0.45}Cr_{0.05}Mn_{1.5}O_4$ at Mn and Ni K edges before and after charge is shown in Fig. 2. The first peak at around 1.5 Å corresponds to the Metal–Oxygen interaction in the first coordination sphere, and the second peak at around 2.5 Å is due to the Metal–Metal interaction in the second coordination sphere. Comparing with pristine $LiNi_{0.5}Mn_{1.5}O_4$, the first peak corresponding to Mn–O interactions in Fig. 2 (left) shows slightly lower intensity in Cr-doped material (Fig. 2, left). The relatively lower peak height could be attributed to the small amount of Mn^{3+} , which was generated after the incorporation of Cr^{3+} and coexisted with Mn^{4+} ions at the 16d site of the spinel structure with two different Mn–O6 coordination octahedra [34]. The second peak in both plots of Fig. 2 corresponds to Mn–M (M = Ni or Mn) and Ni–M interactions. The higher second peak intensity for $LiNi_{0.5}Mn_{1.5}O_4$ in comparison with the Cr-doped $LiNi_{0.45}Cr_{0.05}Mn_{1.5}O_4$ indicates a more ordered local environment of transition metal arrangement in $LiNi_{0.5}Mn_{1.5}O_4$. After charging, the Mn–O peak intensity (Fig. 2, left) increased slightly for the $LiNi_{0.45}Cr_{0.05}Mn_{1.5}O_4$, but remained the same for $LiNi_{0.5}Mn_{1.5}O_4$. This can be explained by the complete oxidation of the Mn^{3+} into Mn^{4+} in $LiCr_{0.05}Ni_{0.45}Mn_{1.5}O_4$ after charge. The most significant local structure change occurs around Ni for both $LiNi_{0.5}Mn_{1.5}O_4$ and $LiNi_{0.45}Cr_{0.05}Mn_{1.5}O_4$, which is due to the oxidation of Ni^{2+} to Ni^{4+} , the major contributor to the charge compensation in the electrochemical activities in spinel.

More quantitatively, EXAFS fitting are performed and the fitted M–O and M–M bond lengths comparing $LiNi_{0.5}Mn_{1.5}O_4$ and $LiNi_{0.45}Cr_{0.05}Mn_{1.5}O_4$ samples before and after charge are listed in Table 1. Cr-doping slightly increases the bond length of Mn–M but decreases Ni–M bonds without influencing significantly on the

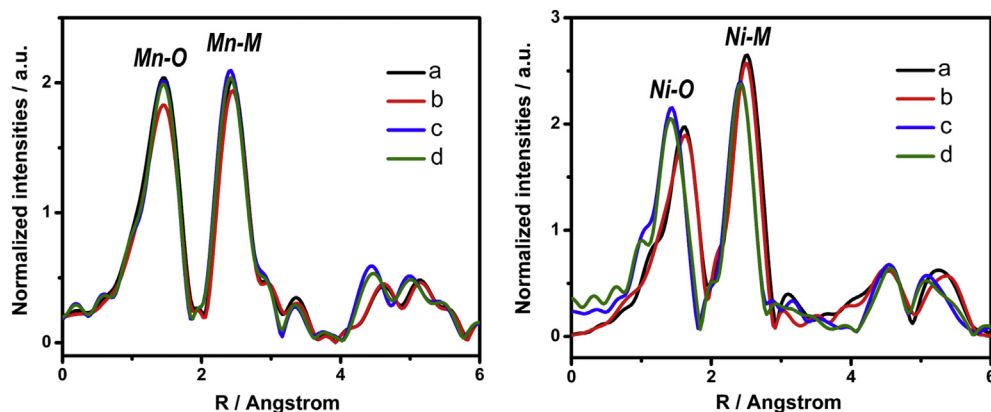


Fig. 2. Magnitudes of Fourier transforms of EXAFS spectra for $LiNi_{0.5}Mn_{1.5}O_4$ and $LiNi_{0.45}Cr_{0.05}Mn_{1.5}O_4$ at Mn (left) and Ni K-edges (Right). a) $LiNi_{0.5}Mn_{1.5}O_4$ and b) $LiNi_{0.45}Cr_{0.05}Mn_{1.5}O_4$ before charge, c) $LiNi_{0.5}Mn_{1.5}O_4$ after charge and d) $LiNi_{0.45}Cr_{0.05}Mn_{1.5}O_4$ after charge.

Table 1

Fitting of Metal–Oxygen and Metal–Metal Bond Lengths in $\text{LiNi}_{0.5}\text{Mn}_{1.5}\text{O}_4$ and $\text{LiNi}_{0.45}\text{Cr}_{0.05}\text{Mn}_{1.5}\text{O}_4$ before and after Charge.

	Mn–O (Å)	Ni–O (Å)	Mn–M (Å)	Ni–M (Å)
$\text{LiNi}_{0.5}\text{Mn}_{1.5}\text{O}_4$	1.893(11)	2.055(18)	2.882(12)	2.909(13)
$\text{LiNi}_{0.5}\text{Mn}_{1.5}\text{O}_4$ -4.9 V	1.894(10)	1.881(7)	2.843(10)	2.806(6)
$\text{LiNi}_{0.45}\text{Cr}_{0.05}\text{Mn}_{1.5}\text{O}_4$	1.892(10)	2.046(15)	2.886(11)	2.902(11)
$\text{LiNi}_{0.45}\text{Cr}_{0.05}\text{Mn}_{1.5}\text{O}_4$ -4.9 V	1.894(11)	1.888(9)	2.850(11)	2.817(8)

Mn–O bonds (Table 1). The Metal–Metal bond length can directly reflect the lattice constant a for cubic $Fd-3m$ structure. Considering Mn is the major framework, the increase of Mn–M bond length after Cr-doping is consistent with the slight increase of the lattice from XRD observation in Fig. 1. After charge, all the bond lengths in Table 1 decrease except Mn–O bond. This is understandable since most of Mn ions are in $4+$ state and electrochemically inactive. The decrease of bond lengths for Ni–O is related with the oxidation of Ni^{2+} to Ni^{4+} , which increases electrostatic force between Ni and O. A closer inspection reveals, however, that the variation of Ni–O bond length in charged states (Table 1) is less in Cr-doped spinel, compared with the undoped one. Therefore, the lattice stress generated from the phase transformation in Cr-doped spinel is alleviated, consistent with *in situ* XRD analysis, which identifies the changes of reaction pathways from two-phase to solid solution reaction after Cr-doping. The observation of the reduced contraction of Ni–O bond lengths during charge also agrees with the aforementioned findings in Fig. 1, where a smaller change of lattice parameter was found in the charged $\text{LiNi}_{0.45}\text{Cr}_{0.05}\text{Mn}_{1.5}\text{O}_4$. The rigid framework, coupled with slightly expanded lattice after Cr-doping, facilitates the fast movement of Li^+ ions during the electrochemical process and minimizes the potential contraction of the unit cell after charge.

The aforementioned crystal structural modifications are further correlated with the electrochemical behaviors for both spinels in Fig. 3. Cyclic voltammogram (CV) curves (Fig. 3a) display signature peaks at 4.0 V for Mn^{3+} , much lower in $\text{LiNi}_{0.5}\text{Mn}_{1.5}\text{O}_4$ than in the doped one and consistent with Fig. 1. The major redox activities originate from $\text{Ni}^{2+}/\text{Ni}^{4+}$ transition between 4.6 and 4.8 V (Fig. 3a). The narrowed voltage gap in $\text{LiNi}_{0.5}\text{Mn}_{1.5}\text{O}_4$ (Fig. 3a) between $\text{Ni}^{2+}/\text{Ni}^{3+}$ and $\text{Ni}^{3+}/\text{Ni}^{4+}$ redox couples was explained by the incommensurateness between the preferred Li/vacancy ordering and Ni/Mn distribution [35], consistent with the relatively flat charge plateau in Fig. 1a. For Cr-doped spinel, a separation into two redox peaks has been discovered, corresponding to the two sloped plateaus in Fig. 1b. The shift of the oxidation peak of $\text{LiNi}_{0.5}\text{Mn}_{1.5}\text{O}_4$ to a higher potential (Fig. 3a) suggests an increased energy barrier for Li^+ ions to leave the host structure. This is probably related with the

more ordered lattice structure and the two-phase reaction throughout the whole charge process of $\text{LiNi}_{0.5}\text{Mn}_{1.5}\text{O}_4$, in contrast to its doped counterpart that contains more disordered phase and wide solid solution regions. The redox peaks for $\text{Cr}^{3+}/\text{Cr}^{4+}$ transitions are seen above 4.8 V, albeit its oxidation peak hidden within the $\text{Ni}^{3+}/\text{Ni}^{4+}$ oxidation process. The increased polarization in $\text{LiNi}_{0.5}\text{Mn}_{1.5}\text{O}_4$ (Fig. 3a) is assigned to the lower conductivity than that of the doped spinel [33]. Intercalation compounds that undergo solid solution reaction usually outperform those experiencing two-phase reactions in terms of their electrochemical properties because of the decreased stress, slower mechanical degradation and reduced number of phase boundaries for Li^+ diffusion in the single-phase behavior. The pronounced advantage of the solid solution transition is further enlarged when comparing the long-term cycling stability of the two spinels in Fig. 3b. Even after 500 cycles, only 12.6% of the original capacity is lost in Cr-doped spinel, while for $\text{LiNi}_{0.5}\text{Mn}_{1.5}\text{O}_4$ a much faster capacity decay is discovered due to the accumulated negative effects from slow two-phase reactions with cycling. Comparison of the rate capabilities for pure and Cr-doped spinels from our previous reports [21,26] also provide further evidences to support the conclusion in this work.

The interplay between two-phase and solid solution transitions are further explained using DFT calculations. Thermodynamically, the excess enthalpy of mixing ΔH_{mixing} , Gibbs free energy of mixing ΔG_{mixing} and entropy of mixing ΔS_{mixing} ($\Delta G_{\text{mixing}} = \Delta H_{\text{mixing}} - T^*\Delta S_{\text{mixing}}$) are often calculated to assess the stability for a given composition within a solid solution series [36,37]. A mixing process with a negative ΔG_{mixing} corresponds to the reaction with energy release, which represents a favorable process. Our quantum–mechanical calculations are carried on the ground state at absolute zero temperature, and thus, $\Delta G_{\text{mixing}} = \Delta H_{\text{mixing}} = \Delta E_{\text{mixing}}$ (ΔE_{mixing} is the excess energy of mixing). The ΔE_{mixing} can be obtained by evaluating the difference between the total energy of the composition $\text{Li}_x\text{Ni}_{0.5}\text{Mn}_{1.5}\text{O}_4$ and the energy of a mechanical mixture of $\text{Ni}_{0.5}\text{Mn}_{1.5}\text{O}_4$ and $\text{LiNi}_{0.5}\text{Mn}_{1.5}\text{O}_4$, which is given by

$$\Delta E_{\text{mixing}} = E(\text{Li}_x\text{Ni}_{0.5}\text{Mn}_{1.5}\text{O}_4) - (1-x)E(\text{Ni}_{0.5}\text{Mn}_{1.5}\text{O}_4) - xE(\text{Ni}_{0.5}\text{Mn}_{1.5}\text{O}_4\text{Li}_1).$$

Fig. 4a–e shows schematic view of a perfect $\text{Ni}_{0.5}\text{Mn}_{1.5}\text{O}_4$ supercell (4a) and Cr substituted $\text{Ni}_{0.5}\text{Mn}_{1.5}\text{O}_4$ supercells (4b–e) denoted by SCr-A, SCr-B, SCr-C and SCr-D, where A, B, C and D denote the substituted sites and S indicates substitution. Fig. 4(f) shows the calculated excess energies of $\text{Li}_x\text{Ni}_{0.5}\text{Mn}_{1.5}\text{O}_4$ with and without Cr-doping as a function of Li content. It can be clearly seen that the calculated excess energies of a perfect $\text{Li}_x\text{Ni}_{0.5}\text{Mn}_{1.5}\text{O}_4$ configuration are always positive, indicating that this configuration

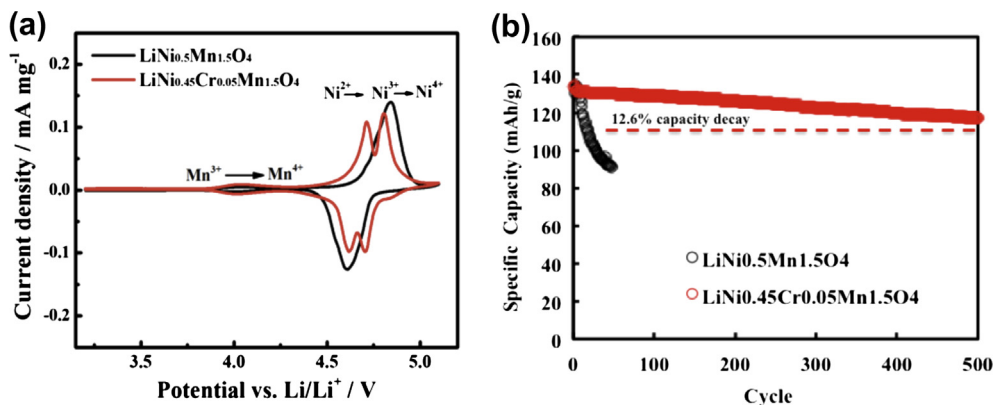


Fig. 3. Comparison of the electrochemical properties of $\text{LiNi}_{0.5}\text{Mn}_{1.5}\text{O}_4$ and $\text{LiNi}_{0.45}\text{Cr}_{0.05}\text{Mn}_{1.5}\text{O}_4$. a) CV and b) Cycling stability at 1C rate between 3.2 and 4.9 V.

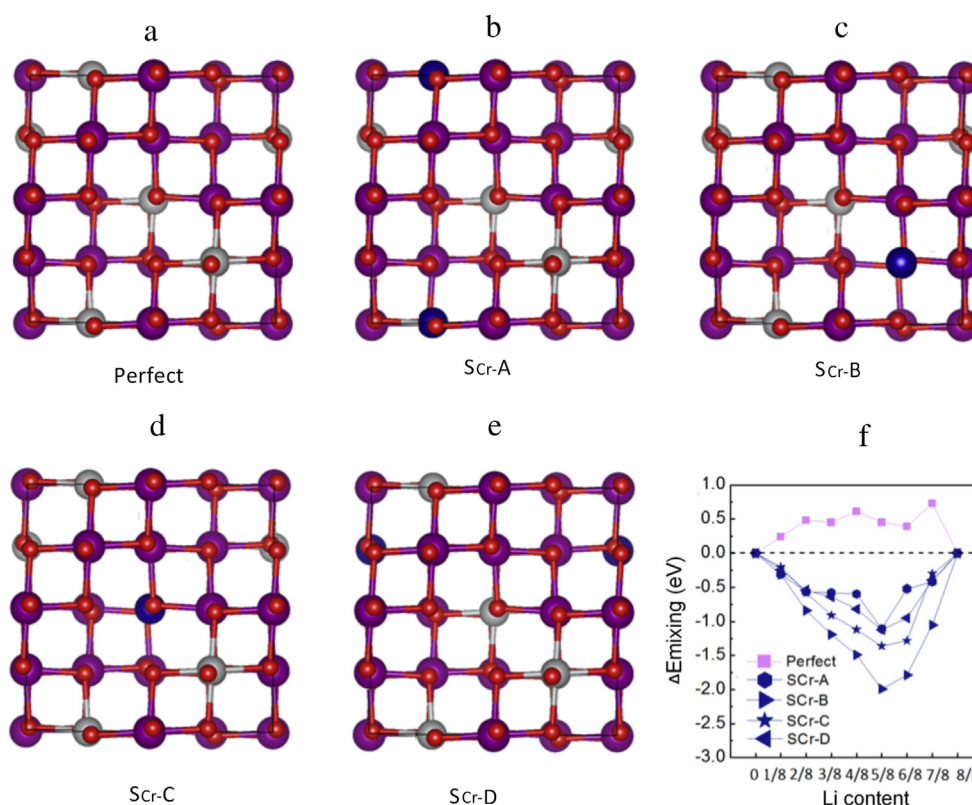


Fig. 4. Schematic view of a) perfect $\text{Ni}_{0.5}\text{Mn}_{1.5}\text{O}_4$ supercell and b)–e) Cr substituted $\text{Ni}_{0.5}\text{Mn}_{1.5}\text{O}_4$ supercell denoted by SCr-A, SCr-B, SCr-C and SCr-D. Here A, B, C and D denote the substituted sites and S indicates substitution. f) The excess energy of mixing (ΔE_{mixing}) for the structures from a) to e) with various Li contents.

is not able to form the solid solution composition for all the Li content. After Cr substitution, the ΔE_{mixing} exhibits a great decrease in energy through the whole range of Li^+ extraction process, leading to more stable solid solution compositions. Although the detailed transition content of Li^+ for forming a solid solution may be slightly different at various temperatures and electrochemical environments, the calculated results are generally consistent with the experimental observations. As a matter of fact, the solubility of Li^+ in $\text{Ni}_{0.5}\text{Mn}_{1.5}\text{O}_4$ may also be due to the expansion of lattice volume after Cr-doping (Fig. 2), leading to the more stable Li^+ in $\text{Ni}_{0.5}\text{Mn}_{1.5}\text{O}_4$ structure.

3. Conclusions

The miscibility gap between two-phase reaction and solid solution reaction in high voltage spinel has been greatly reduced, simply through Cr substitution. Direct evidences from *in situ* XRD and *ex situ* EXAFS demonstrate that after Cr-doping, each of the two two-phase transitions has been largely converted into a solid solution dominated region during charge, leading to the reduced number of phase boundaries for Li^+ transport, alleviated structural stress and mechanical degradation. Accordingly, a significantly improved cycling stability has been achieved in Cr-doped spinel. Thermodynamic stabilities of $\text{Li}_x\text{Ni}_{0.5}\text{Mn}_{1.5}\text{O}_4$ and $\text{Li}_x\text{Ni}_{0.45}\text{Cr}_{0.05}\text{Mn}_{1.5}\text{O}_4$ ($0 \leq x \leq 1$) within a solid solution series are further confirmed by DFT calculations, in an attempt to understand the interplay between the different phase transition reaction pathways, which are directly related with the improved cycling stability of Cr-doped spinel. This work provides insights to unlock the topotactic nature of intercalation compounds thus appropriate strategies may be developed to modulate the crystal lattices for energy storage applications.

Acknowledgment

This work was supported by the Assistant Secretary for Energy Efficiency and Renewable Energy, Office of Vehicle Technologies of the U.S. Department of Energy under Contract No. DE-AC02-05CH11231, Subcontract No 18769 under the Batteries for Advanced Transportation Technologies (BATT) Program. The work at Brookhaven National Laboratory was supported by DOE, the Assistant Secretary for Energy Efficiency and Renewable Energy, Office of Vehicle Technologies under Contract Number DE-AC02-98CH10886. The authors acknowledge technical supports by the NSLS's Beamline scientists at X18A, Drs. Steve Ehrlich, Syed Khalid, Qi Wang, and Nebojsa Marinkovic. The electron microscopy was conducted in the William R. Wiley Environmental Molecular Sciences Laboratory (EMSL), a national scientific user facility sponsored by DOE's Office of Biological and Environmental Research and located at PNNL.

Appendix A. Supplementary material

Supplementary material related to this article can be found at <http://dx.doi.org/10.1016/j.jpowsour.2013.05.148>.

References

- [1] J.-M. Tarascon, M. Armand, *Nature* 414 (2001) 359–367.
- [2] M. Stanley Whittingham, *IEEE Proc.* 100 (2012) 1518.
- [3] J.B. Goodenough, Y. Kim, *Chem. Mater.* 22 (2010) 587.
- [4] L.-X. Yuan, Z.-H. Wang, W.-X. Zhang, X.-L. Hu, J.-T. Chen, Y.-H. Huang, J.B. Goodenough, *Energy Environ. Sci.* 4 (2011) 269.
- [5] M. Stanley Whittingham, *Chem. Rev.* 104 (2004) 4271.
- [6] N. Meethong, H.Y.S. Huang, W.C. Carter, Y.M. Chiang, *Electrochem. Solid-State Lett.* 10 (2007) A134.
- [7] C. Delacourt, P. Poizot, J.-M. Tarascon, C. Masquelier, *Nat. Mater.* 4 (2005) 254.

- [8] N. Sharma, X. Guo, G. Du, Z. Guo, J. Wang, Z. Wang, V.K. Peterson, *J. Am. Chem. Soc.* 134 (2012) 7867.
- [9] Y.J. Lee, C. Eng, C.P. Grey, *J. Electrochem. Soc.* 148 (2001) A249.
- [10] L. Wang, H. Li, X. Huang, E. Baudrin, *Solid State Ionics* 193 (2011) 32.
- [11] T.-F. Yi, Y. Xie, M.F. Ye, L.-J. Jiang, R.-S. Zhu, Y.-R. Zhu, *Ionics* 17 (2011) 383.
- [12] S. Rajakumar, R. Thirunakaran, A. Sivashanmugam, J. Yamaki, S. Gopukumar, *J. Electrochem. Soc.* 156 (2009) A246.
- [13] J. Cabana, H. Zheng, A.K. Shukla, C. Kim, V.S. Battaglia, M. Kunduraci, *J. Electrochem. Soc.* 158 (2011) A997.
- [14] M. Kunduraci, G.G. Amatucci, *J. Electrochem. Soc.* 153 (2006) A1345.
- [15] K. Ariyoshi, Y. Maeda, T. Kawai, T. Ohzuku, *J. Electrochem. Soc.* 158 (2011) A281.
- [16] Z. Chen, S. Qiu, Y. Cao, X. Ai, K. Xie, X. Hong, H. Yang, *J. Mater. Chem.* 22 (2012) 11768.
- [17] J. Gao, J. Li, C. Jiang, C. Wan, *J. Electrochem. Soc.* 157 (2010) A899.
- [18] K.M. Shaju, P.G. Bruce, *Dalton Trans.* 5471 (2008).
- [19] J.-H. Kim, S.-T. Myung, C.S. Yoon, S.G. Kang, Y.-K. Sun, *Chem. Mater.* 16 (2004) 906.
- [20] L.H. Chi, N.N. Dinh, S. Brutti, B. Scrosatti, *Electrochim. Acta* 55 (2010) 5110.
- [21] D. Liu, J. Han, M. Dongtigny, P. Charest, A. Guerfi, K. Zaghib, J.B. Goodenough, *J. Electrochem. Soc.* 157 (2010) A770.
- [22] J. Zheng, J. Xiao, X. Yu, L. Kovarik, M. Gu, F. Omenya, X. Chen, X.-Q. Yang, J. Liu, G.L. Graff, M.S. Whittingham, J.-G. Zhang, *Phys. Chem. Chem. Phys.* 14 (2012) 13515.
- [23] S.B. Park, W.S. Eom, W.I. Cho, H. Jang, *J. Power Sources* 159 (2006) 679–684.
- [24] J. Liu, A. Manthiram, *J. Electrochem. Soc.* 156 (2009) A66.
- [25] M. Aklalouch, R.M. Rojas, J.M. Rojo, I. Saadoun, J.M. Amarilla, *Electrochim. Acta* 54 (2009) 7542.
- [26] J. Xiao, X. Chen, P.V. Sushko, M.L. Sushko, L. Kovarik, J. Feng, Z. Deng, J. Zheng, G.L. Graff, Z. Nie, D. Choi, J. Liu, J.-G. Zhang, M.S. Whittingham, *Adv. Mater.* 24 (2012) 2109.
- [27] D. Liu, Y. Lu, J.B. Goodenough, *J. Electrochem. Soc.* 157 (2010) A1269.
- [28] G.B. Zhong, Y.Y. Wang, Z.C. Zhang, C.H. Chen, *Electrochim. Acta* 56 (2011) 6554.
- [29] B. Ravel, M. Newville, *J. Synchrotron Radiat.* 12 (2005) 537.
- [30] J.J. Rehr, S.I. Zabinsky, R.C. Albers, *Phys. Rev. Lett.* 69 (1992) 3397.
- [31] X. Chen, W. Xu, J. Xiao, M.H. Engelhard, F. Ding, D. Mei, D. Hu, J. Zhang, J.-G. Zhang, *J. Power Sources* 213 (2012) 160.
- [32] J. Zheng, J. Xiao, W. Xu, X. Chen, M. Gu, X. Li, J.-G. Zhang, *J. Power Sources* 227 (2013) 211.
- [33] S. Patoux, L. Daniel, C. Bourbon, H. Lignier, C. Pagano, F. Le Cras, S. Jouanneau, S. Martinet, *J. Power Sources* 189 (2009) 344.
- [34] Y. Shiraishi, I. Nakai, T. Tsubata, T. Himeda, F. Nishikawa, *J. Solid State Chem.* 133 (1997) 587.
- [35] E. Lee, K.A. Persson, *Energy Environ. Sci.* 5 (2012) 6047.
- [36] E.D.A. Ferriss, R.C. Ewing, U. Becker, *Am. Mineral.* 95 (2010) 229.
- [37] X.J. Wang, H.Y. Xiao, X.T. Zu, W.J. Weber, *J. Nucl. Mater.* 424 (2012) 69.